Geochemistry, Geophysics, Geosystems®

RESEARCH ARTICLE
10.1029/2021GC010182

Multi-Band Raman Analysis of Radiation Damage in Zircon for Thermochronology: Partial Annealing and Mixed Signals

Birk Härtel[1], Raymond Jonckheere[1], and Lothar Ratschbacher[1]

[1]Geologie, TU Bergakademie Freiberg, Freiberg, Germany

Key Points:

- Annealing and inhomogeneous damage are two main factors hindering radiation-damage estimation for zircon Raman dating
- Comparison of internal and external Raman bandwidths allows to detect partial annealing of radiation damage in zircon
- Comparison of internal Raman bandwidths allows to detect artifactual broadening in zoned zircon

Supporting Information:

Supporting Information may be found in the online version of this article.

Correspondence to:

B. Härtel,
haertelb@mailserver.tu-freiberg.de

Citation:

Härtel, B., Jonckheere, R., & Ratschbacher, L. (2022). Multi-band Raman analysis of radiation damage in zircon for thermochronology: Partial annealing and mixed signals. *Geochemistry, Geophysics, Geosystems*, *23*, e2021GC010182. https://doi.org/10.1029/2021GC010182

Received 22 SEP 2021
Accepted 5 JAN 2022

Author Contributions:

Conceptualization: Birk Härtel
Formal analysis: Birk Härtel, Raymond Jonckheere
Investigation: Birk Härtel
Methodology: Birk Härtel
Supervision: Raymond Jonckheere, Lothar Ratschbacher
Visualization: Birk Härtel
Writing – original draft: Birk Härtel
Writing – review & editing: Raymond Jonckheere, Lothar Ratschbacher

Abstract Four zircon Raman bands were previously calibrated to give consistent estimates of the accumulated self-irradiation α-dose in unannealed volcanic samples. Partial annealing of radiation damage produces inconsistent values because of differences in the relative annealing sensitivities. The damage estimates based on the external rotation band (D_{ER}) at ∼356 cm^{-1} and that based on the $\nu_2(SiO_4)$ band (D_2) at ∼438 cm^{-1} are the most and least sensitive to damage annealing. The D_2/D_{ER}-ratio thus provides a numerical estimate of the extent of geologic annealing that a zircon sample has experienced. This ratio characterizes the thermal history of a zircon sample but also its state of radiation damage during the course of its geologic history, and thus the manner in which this state influences other thermochronologic methods. Meaningful interpretation of the zircon Raman age requires that the spectra are free of measurement artifacts. The major artifacts result from micrometer-scale gradients of the damage densities within a zircon grain due to uranium and thorium zoning. The micrometer-sized sampled volume may span different densities, producing overlapping spectra, causing apparent peak broadening, overestimated damage densities, and zircon Raman ages. The D_3/D_2-ratio of the damage densities calculated from the $\nu_3(SiO_4)$ and $\nu_2(SiO_4)$ bands, most and least affected by overlap, is an efficient indicator of a meaningless signal. It reveals overlap in annealed and unannealed samples, because the used bands have similar responses to annealing. Multi-band Raman maps can be converted to damage-ratio maps for screening zircon mounts, and selecting spots for thermochronologic investigations.

Plain Language Summary Radioactive processes cause damage to the lattice of zircon crystals. This damage can be measured with a Raman instrument. Such measurements are important for methods determining the ages and thermal histories of zircon grains in rocks. Thus, the Raman measurements must be reliable and meaningful. This work proposes tools for detecting effects that hinder the interpretation of zircon Raman data. These effects are mixed signals and loss of damage due to exposure to elevated temperatures in the geologic environment. Zircon Raman spectra have different bands that respond differently to mixed signals and temperature. The ratio of the damage estimates from the least and most temperature-sensitive bands thus indicates partial annealing. Raman spectra of zoned zircons often straddle areas with different lattice damage. Their overlapping signals cause artificial band broadening, and a damage overestimation. The ratio of the damage estimated from the least and the most affected bands identifies mixed signals and allows to reject unsuitable samples. The damage ratios can also be plotted in maps for damage screening and for selecting optimal spots for measurements.

1. Introduction

Thermochronology studies the timing and rates of geologic phenomena based on the radioactive processes occurring within natural minerals. At the same time, these processes damage the mineral, changing its properties over time. Measurements of self-irradiation damage are thus an important part of thermochronologic studies. Such measurements broke ground for: (a) zircon Raman dating, in which the self-irradiation damage itself is a measure of the age of the sample (Härtel, Jonckheere, Wauschkuhn, Hofmann, et al., 2021; Pidgeon, 2014); (b) the refinement of thermochronometers, whose results are influenced by self-irradiation damage, for example, (U-Th)/He dating (Anderson et al., 2020; Guenthner et al., 2013); and (c) the applicability of provenance studies, using Raman characteristics of detrital zircons to distinguish thermal histories (Garver & Davidson, 2015; Resentini et al., 2020).

Zircon ($ZrSiO_4$) substitutes U and Th for Zr in its structure. Disintegration of ^{238}U, ^{235}U, ^{232}Th, and their daughters damages the lattice by the emission of α-particles and the recoil of the daughter nuclei (Bohr, 1948; Joly, 1907; Mügge, 1922). An α-particle displaces ∼10^2 atoms toward the end of its ∼10–20 μm trajectory through the

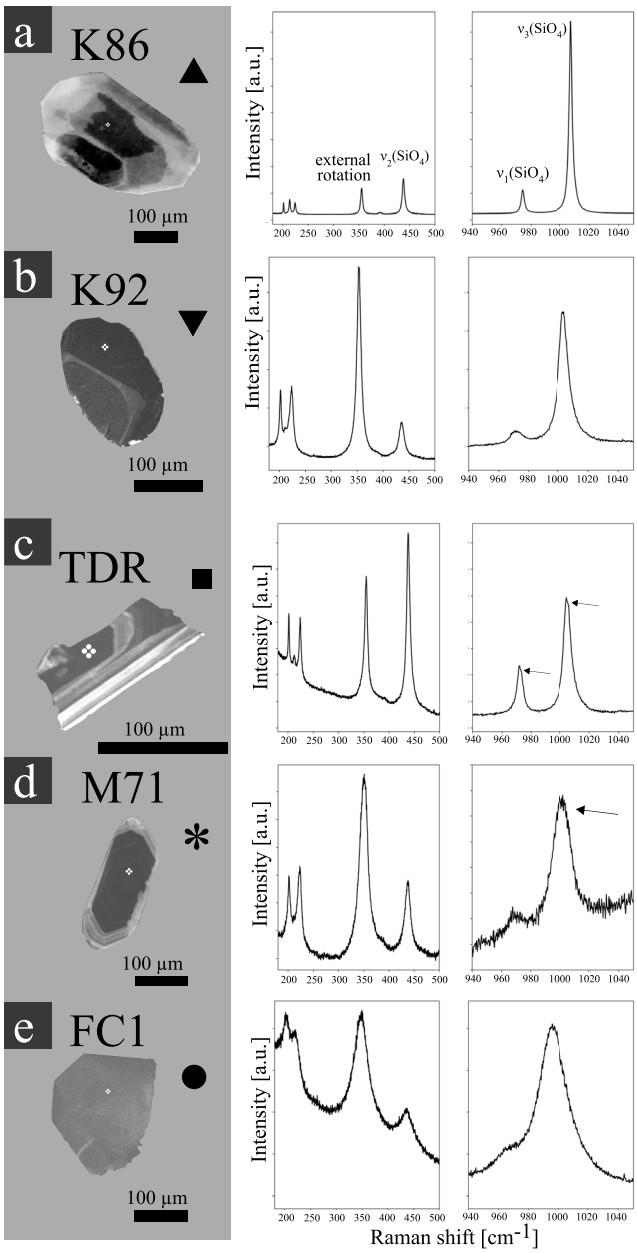

Figure 1. Cathodoluminescence (CL) images and Raman spectra of zircon from samples (a) K86, (b) K892, (c) TDR, (d) M71, and (e) FC1 zircon. Panels (a and b) show typical symmetric Raman peaks in partially annealed zircons. The peaks marked by arrows in panels (c and d) show asymmetric or rounded shapes. The white dots in the CL images mark the Raman spots. The symbols (▲, ▼, ■, ✻, and ●) identify the spectra in the subsequent figures. Band assignment after Kolesov et al. (2001).

crystal (Nasdala et al., 2001), whereas the recoiling daughter nucleus creates an amorphous recoil track, displacing ~10^3 atoms along its ~20 nm long path (Jonckheere & Gögen, 2001; Nasdala et al., 2001; Salje & Farnan, 2001; Trachenko et al., 2003). This self-irradiation damage causes swelling of the zircon unit cell, and an increase of disorder in the lattice, in the end causing the amorphization of the crystal (Holland & Gottfried, 1955; Murakami et al., 1991). Upon heating, radiation damage anneals through several stages until the crystal reaches a well-ordered state similar to that of undamaged zircon (Colombo & Chrosch, 1998; Geisler, 2002; Geisler et al., 2001). Stage I annealing is usually interpreted as shrinking of the unit cell perpendicular to the ***c***-axis and the elimination of point defects, whereas in stage II the amorphous domains crystallize (Colombo & Chrosch, 1998; Geisler et al., 2001). Geisler (2002) defined a third annealing stage, in which the remaining, most stable point defects are eliminated.

Nasdala et al. (1995) used Raman spectroscopy for non-destructive, high-resolution radiation-damage measurements in zircon. The Raman peaks widen (full width at half-maximum; Γ [cm^{-1}]) and shift position (ω [cm^{-1}]) to lower wavenumbers with increasing damage (Figure 1; Nasdala et al., 1995, 1998; Zhang et al., 2000). The accumulated damage is commonly expressed in terms of the number of α-events that have occurred since the zircon's formation (α-dose; D_α [α/g]). The relationship between ω and Γ with increasing α-dose is shown by the gray dashed lines in the diagrams of Figure 2 for the $\nu_1(SiO_4)$, $\nu_2(SiO_4)$, $\nu_3(SiO_4)$ bands, and the external rotation (ER) band at Raman shifts (ω) of ~974, 438, 1,008, and 356 cm^{-1}. Nasdala et al. (2001) calibrated the width of the $\nu_3(SiO_4)$ band (Γ_3) against the α-dose calculated from the U and Th concentrations and the U/Pb ages of a set of unannealed zircons. Härtel, Jonckheere, Wauschkuhn, Hofmann, et al. (2021) made a comparable calibration of the $\nu_1(SiO_4)$, $\nu_2(SiO_4)$, $\nu_3(SiO_4)$, and ER bandwidths as a function of D_α for a set of unannealed volcanic zircons of different ages.

For unannealed samples, there exists a linear relationship between the Raman bandwidths and the α-dose:

$$D(\alpha/\mathrm{g}) = \frac{\Gamma(\mathrm{cm}^{-1}) - \Gamma_0(\mathrm{cm}^{-1})}{\Delta\Gamma/\Delta D(\mathrm{g/cm}^{-1})}, \quad (1)$$

wherein Γ_0 is the Raman bandwidth of an undamaged zircon, and $\Delta\Gamma/\Delta D$ the dose response, the change in bandwidth as a function of D_α. The α-dose can thus be estimated from each band for which Γ_0 and $\Delta\Gamma/\Delta D$ have been determined; Table 1 lists the recent values of Härtel, Jonckheere, Wauschkuhn, Hofmann, et al. (2021).

Zircon Raman dating determines the time (t) over which the radiation damage accumulated from its measurement by Raman (Equation 1) and the accumulation rate, which is proportional to the effective uranium concentration (eU = 1.04 [U] + 0.24 [Th]). The apparent zircon Raman age is given by (Härtel, Jonckheere, Wauschkuhn, Hofmann, et al., 2021):

$$t \approx 3.19 \cdot 10^{-19}(\mathrm{Ma\,g/\alpha})\frac{D(\alpha/\mathrm{g})}{eU\,(\mathrm{g/g})}. \quad (2)$$

Annealing lowers Γ (Geisler, 2002; Geisler et al., 2001; Ginster et al., 2019) and therefore D (Equation 1) does not correspond to the α-dose but to a dose equivalent to a lower degree of radiation damage. This also causes a decrease in t (Equation 2). A sample's thermal history thus determines the geologic meaning of its apparent age (Wagner, 1981). Rapid cooling to temperatures where no annealing takes place gives an event age. In the case

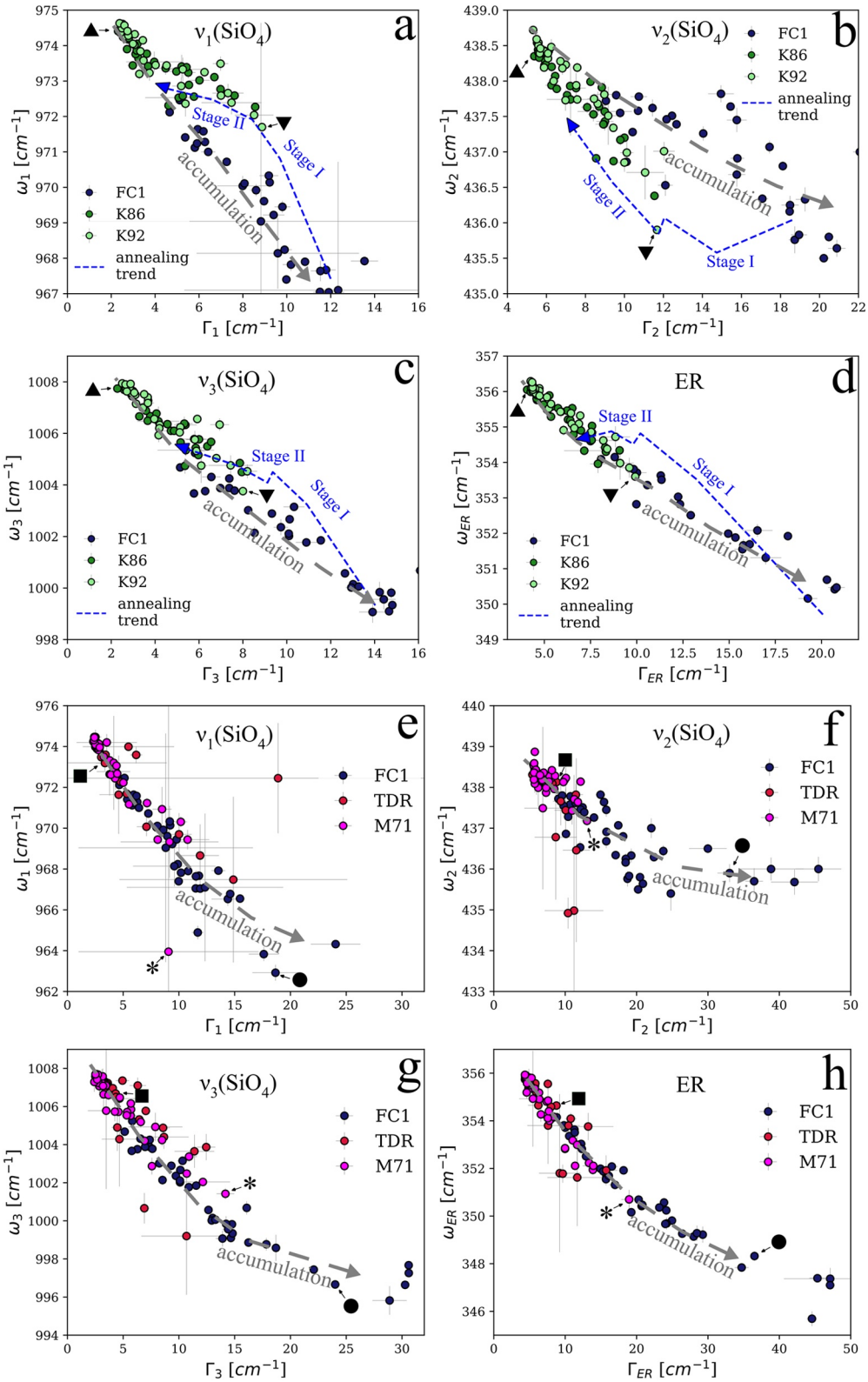
a
$\nu_1(SiO_4)$
ω_1 [cm^{-1}]
Γ_1 [cm^{-1}]
b
$\nu_2(SiO_4)$
ω_2 [cm^{-1}]
Γ_2 [cm^{-1}]
c
$\nu_3(SiO_4)$
ω_3 [cm^{-1}]
Γ_3 [cm^{-1}]
d
ER
ω_{ER} [cm^{-1}]
Γ_{ER} [cm^{-1}]
e
$\nu_1(SiO_4)$
ω_1 [cm^{-1}]
Γ_1 [cm^{-1}]
f
$\nu_2(SiO_4)$
ω_2 [cm^{-1}]
Γ_2 [cm^{-1}]
g
$\nu_3(SiO_4)$
ω_3 [cm^{-1}]
Γ_3 [cm^{-1}]
h
ER
ω_{ER} [cm^{-1}]
Γ_{ER} [cm^{-1}]
FC1
K86
K92
annealing trend
TDR
M71
Stage I
Stage II
accumulation

Figure 2.

Table 1
Radiation-Damage Calibration

Raman band	$\Delta\omega/\Delta D$ (10^{-16} g/cm α)	$\Delta\Gamma/\Delta D$ (10^{-16} g/cm α)	Γ_0 (cm^{-1})
$\nu_1(SiO_4)$	−0.07	0.11	1.96
$\nu_2(SiO_4)$	−0.02	0.14	5.16
$\nu_3(SiO_4)$	−0.08	0.11	2.85
ER	−0.06	0.17	4.04

Note. Dose responses of the bandwidths ($\Delta\Gamma/\Delta D$) and band positions ($\Delta\omega/\Delta D$), and zero-damage bandwidths (Γ_0) of four zircon Raman bands (Härtel, Jonckheere, Wauschkuhn, Hofmann, et al., 2021).

of gradual cooling, the age dates the crossing of a specific closure temperature (T_c; Dodson, 1973). Härtel, Jonckheere, Wauschkuhn, and Ratschbacher (2021) estimated that $T_c \approx 330°C–370°C$ for zircon Raman ages calculated from Γ_2 and Γ_3, and $T_c \approx 260°C–310°C$ for those calculated from Γ_{ER}. A sample reheated to the point of complete repair gives a reset age. In the case of incomplete annealing, the age is a mixed age that does not date a specific geologic event. The different closure temperatures of different Raman bands create the potential for multi-T_c zircon Raman dating.

Diffusion experiments show that the closure temperature of zircon (U-Th)/He dating changes with the accumulated radiation damage (Guenthner et al., 2013). T_c increases up to $D \approx 200{\cdot}10^{16}$ α/g but plummets at higher values due to the opening up of fast He diffusion pathways caused by the percolation of amorphous domains (Guenthner et al., 2013; Salje et al., 1999). The drop in He retention at high α-doses is corroborated by mapping He concentrations in zoned zircons showing high variation of eU across zones (Danišik et al., 2017). Recent studies on zircon (U-Th)/He dating (Anderson et al., 2020; Hueck et al., 2018) use Raman measurements for monitoring radiation damage for improving the interpretation of (U-Th)/He ages. Ginster (2018) reported that radiation-damage annealing also changes He diffusion parameters compared unannealed zircons.

Raman spectroscopy is used in provenance studies for distinguishing detrital zircons based on their damage accumulation and annealing signatures. Garver and Davidson (2015) and Resentini et al. (2020) compared the damage measured with Raman to the α-dose calculated from the U and Th contents and the U/Pb age. If the Raman measurements indicate lower damage than expected from the α-dose, annealing must have taken place either during cooling or reheating. Nasdala et al. (2014) used this approach for investigating the annealing of zircon xenocrysts in a kimberlite diatreme. The comparison of α-dose and Raman parameters reveals whether or not lattice repair has taken place but not its timing, duration, or temperature; neither does it distinguish between partial and complete repair. Because of the low temperatures needed for annealing, it is likely the rule rather than the exception. The partial annealing zones for different zircon Raman bands go down to ~180°C (Härtel, Jonckheere, Wauschkuhn, & Ratschbacher, 2021); Jonckheere et al. (2019) observed partial annealing of zircons from the KTB borehole at *in situ* temperatures down to ~100°C.

Annealing complicates the interpretation of zircon Raman measurements. Geisler et al. (2001) proposed the distinct accumulation (Figure 2c; gray dashed line) and annealing paths (blue dashed line) in the ω_3-Γ_3 plot for recognizing annealing: annealing is not the reverse of accumulation and each process has its own signature in the ω_3-Γ_3 plot. Annealing proceeds in stages: ω_3 changes most during stage I, while Γ_3 is most affected during stage II. Ginster et al. (2019) corroborated this result, and Härtel, Jonckheere, Wauschkuhn, and Ratschbacher (2021) found similar trends for the $\nu_1(SiO_4)$, $\nu_2(SiO_4)$, and ER bands (Figure 2). Nasdala et al. (2002) and Jonckheere et al. (2019) observed annealing signatures in natural zircons. Raman spectra of partially annealed zircons show symmetric cusped peaks that are indistinguishable from those of unannealed zircons (Figures 1a and 1b). Peak fitting reveals however that their positions (ω) and widths (Γ) are not consistent with the accumulation lines (Figures 2a–2d, samples ▲ and ▼; Geisler et al., 2001; Härtel, Jonckheere, Wauschkuhn, Hofmann, et al., 2021; Zhang et al., 2000).

Radiation-damage measurements by Raman are also affected by mixed signals due to actinide zoning in minerals. Actinide zoning produces abrupt jumps and steep gradients of the radiation damage at the micrometer scale, causing signals from the more- and less-damaged zones to overlap. The resulting peak broadening depends on the damage contrasts in the sampled volume and the respective Raman intensities, and leads to overestimated bandwidths and damage densities (Geisler & Pidgeon, 2002; Kempe et al., 2018; Nasdala et al., 2001, 2005). Zircons that appear homogeneous in BSE (back-scatter-electron) and CL (cathodoluminescence) images can nevertheless yield mixed Raman signals, if the sampled depth crosses zone boundaries (Nasdala et al., 2005).

Figure 2. Plots of band position (ω) versus bandwidth (Γ) for the (a) $\nu_1(SiO_4)$, (b) $\nu_2(SiO_4)$, (c) $\nu_3(SiO_4)$, and (d) external rotation (ER) Raman bands of the partially annealed samples K86 and K92; and for the (e) $\nu_1(SiO_4)$, (f) $\nu_2(SiO_4)$, (g) $\nu_3(SiO_4)$, and (h) ER Raman bands of the samples TDR and M71 showing band overlap. Sample FC1 is shown in every plot for comparison. The gray dashed lines are the radiation-damage accumulation trends based on the FC1 data. The blue dashed lines show the annealing trends for isothermal annealing of a zircon with an accumulated damage of 10^{18} α/g (Härtel, Jonckheere, Wauschkuhn, & Ratschbacher, 2021). Symbols ▲, ▼, ■, ✻, and ● mark the data points corresponding to the spectra in Figure 1. Error bars are 2σ.

Figures 1c and 1d show CL images and Raman spectra of zircon grains, with the laser spots placed in apparently homogeneous areas. In contrast to the symmetrical, well-shaped peaks in Figures 1a and 1b, Figure 1c shows a spectrum with right-skewed $\nu_1(SiO_4)$ and $\nu_3(SiO_4)$ Raman peaks (arrows), whereas the $\nu_2(SiO_4)$ and the ER peaks are symmetric. Figure 1d shows a round-topped $\nu_3(SiO_4)$ peak (arrow) that deviates from the cusped Lorentz or Voigt shape; this indicates overlapping signals of comparable-strength signals, combined into a broadened symmetric band (Kempe et al., 2018; Nasdala et al., 2005). In contrast, the $\nu_2(SiO_4)$ and ER bands have the typical cusped peak shapes. Figure 1e shows the Raman spectrum of a high-damage zircon ($D \approx 2{\cdot}10^{18}$ α/g) with a broad $\nu_3(SiO_4)$ peak, but where the $\nu_2(SiO_4)$ and ER peaks are broadened as well. The apparent left tail of the $\nu_3(SiO_4)$ peak is in part due to its fusion with the adjoining $\nu_1(SiO_4)$ band.

The common method for detecting overlap is visual inspection of the spectrum and of the peak fitting residuals. This depends on the spectral resolution of the equipment, the Raman background, and the signal-to-noise ratio (Saltonstall et al., 2019). Some investigators fitted overlapping peaks with two or more peak functions per Raman band (e.g., Geisler & Pidgeon, 2002; Kempe et al., 2018; Nasdala et al., 2002); this is however not useful for interpreting such fits in terms of radiation damage.

Annealing and overlap prevent a confident interpretation of zircon Raman spectra in terms of radiation damage. Based on a multi-band approach, we propose numerical criteria for detecting annealing and band overlap: we introduce the damage-estimate ratios (D/D) for the $\nu_2(SiO_4)$, $\nu_3(SiO_4)$, and ER bands, and show that a D_2/D_{ER} average >1 or a significant fraction of the grains outside the statistical limits of the measurement errors indicate that the entire population experienced partial annealing. We also show that the D_3/D_2-ratio indicates a mixed signal, arising from a sampled volume that includes different damage densities. A $D_3/D_2{-}D_2$ plot permits to distinguish the systematic overlap effect from statistical scatter. Finally, we present multi-band Raman maps, converted to D/D-ratio maps, and demonstrate that they can be interpreted in terms of both overlap and annealing. We present a protocol for Raman radiation-damage measurements that includes the annealing and mixed-signal detection. With these improvements, Raman measurements can produce robust and valid estimates of the accumulated radiation damage and its annealing for the purpose of zircon Raman dating, and should become essential aspects of other thermochronologic applications, in particular (U-Th)/He dating.

2. Materials and Methods

2.1. Samples

We investigated the Raman signature of partial annealing of zircons from two orthogneisses in the Katha range in Myanmar (K86 and K92; Figures 1a and 1b). Their igneous, likely hypabyssal protoliths crystallized in the Early Cambrian and underwent Paleocene greenschist-to amphibolite-facies metamorphism. Based on our estimates of the zircon radiation-damage partial annealing zones for the different Raman bands (Härtel, Jonckheere, Wauschkuhn, & Ratschbacher, 2021), a significant fraction of the damage accumulated before metamorphism must have annealed. We investigated band overlap in zircon from the Tardree rhyolite fission track age standard (TDR; Hurford, 1990, Figure 1c), emplaced during the early Paleocene and not reheated afterward (Green, 1985; Hurford & Green, 1983; CA-TIMS zircon $^{238}U/^{206}Pb$ age: 61.32 ± 0.09 Ma, Ganerød et al., 2011). We also investigated band broadening in zircons from an Eocene, hornblende-bearing granite from the Mogok Belt in Myanmar (M71; Figure 1d); Text S1 and S2 in Supporting Information S1 summarize relevant data for the Myanmar samples. TDR and M71 have strong radiation damage zoning and some spectra are thus expected to exhibit band overlap (Figures 1c and 1d). For comparison, we also studied zircons from the Neoproterozoic Duluth Complex anorthosites, Minnesota (FC1; Figure 1e; CA-ID-TIMS zircon $^{207}Pb/^{206}Pb$ age: 1,099.0 ± 0.6 Ma, Paces and Miller, 1993). These are homogeneous in CL, show no reaction textures, span a broad range of radiation damage (Marillo-Sialer et al., 2016), and did not experience reheating after initial cooling according to apatite fission track data (Iwano et al., 2019). We thus expect them to show neither artifactual band broadening nor annealing. For Raman mapping, we used a 3 by 1.8 mm, zoned zircon grain from the Plešovice reference material (zircon $^{238}U/^{206}Pb$ age from multiple methods: 337.13 ± 0.37 Ma, Sláma et al., 2008), whose exhumation history has not been studied in detail yet.

2.2. Raman Spectrometry

We recorded the Raman spectra in single mode with a TriVista spectrometer (Princeton Instruments; Spectroscopy & Imaging) built around an Olympus BX51W1 microscope with a 100× objective (n.a. 0.75). We used a Coherent Sapphire SF NX 488 nm laser with ∼12 mW power at the sample surface. The spectral resolution is ∼0.8 cm^{-1} at a pixel resolution of ∼0.2 cm^{-1}. The spot size on the sample surface was 1–2 μm; the height of the sampled volume ∼5 μm. We recorded each spectrum in 10 acquisitions of 10 s. Repeat measurements on three slightly to moderately radiation-damaged reference zircons ($\Gamma_3 \approx$ 7–20 cm^{-1}) showed no changes of the Raman parameters due to the laser irradiation. We calibrated the instrument using the 219.2 cm^{-1} sulfur, 520.7 cm^{-1} silicon, and 1,001.4 cm^{-1} polystyrene bands. Each spectrum spans the wavenumber interval 170–1,100 cm^{-1}, and was recorded in three steps using a step-and-glue algorithm. We extracted three Raman band groups (170–260, 300–520, and 940–1,050 cm^{-1}), to which we fitted a third-order-polynomial background and Lorentz functions for determining the peak positions (ω) and widths (Γ), using a Python script written for this purpose and tested on the calibration data of Härtel, Jonckheere, Wauschkuhn, Hofmann, et al. (2021). We used the method of Tanabe and Hiraishi (1980) to corrected for instrumental broadening. To allow for small-scale heterogeneities, we measured sets of four spots, ∼5 μm apart; we report their mean positions and widths, and half the maximum deviation from the means as 1σ-error.

We mapped the Plešovice zircon grain using a 30-μm rectangular grid in two runs: first the interval 170–500 cm^{-1} and then 800–1,100 cm^{-1}. Each spectrum was recorded in 10 acquisitions of 10 s using the 50× objective (n.a. 0.75) and 0.8 mW laser power to avoid damage to the epoxy mount. We carried out the peak fitting and instrumental correction as for the spot measurements. Tables S1 and S2 summarize the results.

3. Results and Discussion

3.1. Partial Annealing

Figures 2a–2d plot ω against Γ for the four most intense zircon Raman bands of K86 and K92, and FC1. The FC1 data define a damage accumulation trend of decreasing ω with increasing Γ (gray dashed lines; Geisler et al., 2001). Γ_1 and Γ_3 for FC1 range up to 25 and 30 cm^{-1}, and Γ_2 and Γ_{ER} up to 47 cm^{-1} (Figures 2e–2h). For all four bands, ω levels off at high Γ values (Härtel, Jonckheere, Wauschkuhn, Hofmann, et al., 2021; Zhang et al., 2000). The ω-ranges are ∼3 cm^{-1} for ω_2, ∼10 cm^{-1} for ω_{ER}, and ∼12 cm^{-1} for ω_1 and ω_3. In contrast, the bandwidths of K86 and K92 only range up to 9 (Γ_1), 12 (Γ_2), 8 (Γ_3), and 10 cm^{-1} (Γ_{ER}), whereas the range of their peak positions is between 2 and 2.5 cm^{-1} (ω_1, ω_2, and ω_{ER}) or ∼4 cm^{-1} (ω_3).

The K86 and K92 data lie off the accumulation lines for all four bands, close to the segments of the annealing lines associated with stage II (Figures 2a–2d; blue dashed lines; Geisler et al., 2001). The ω-Γ plots thus allow to detect partial annealing, as reported for $\nu_3(SiO_4)$ by Geisler et al. (2001), Nasdala et al. (2002), Jonckheere et al. (2019), and Härtel, Jonckheere, Wauschkuhn, and Ratschbacher (2021). The offsets from the accumulation lines of $\nu_3(SiO_4)$ and ER are less obvious because their annealing lines are closer to their accumulation lines than those of $\nu_1(SiO_4)$ and $\nu_2(SiO_4)$. The closeness of the stage II and accumulation lines of all bands makes it difficult to detect annealing in the ω-Γ plots, in particular when new damage accumulates after a natural heating event.

Figure 3 plots ω_1 (a), ω_3 (b), and ω_{ER} (c) against ω_2 for K86, K92, and FC1. In contrast to the ω–Γ plots, the ω–ω plots take advantage of the different annealing paths with respect to ω of the different Raman bands and the clear separation between the accumulation and annealing lines of ω_2 (Figure 2b). Damage accumulation lowers the ω of all bands. During annealing, ω_1, ω_3, and ω_{ER} show the greatest increases during stage I, while ω_2 decreases in stage I and increases in stage II (blue dashed line). The FC1 data define a diffuse accumulation trend (gray dashed lines). The K86 and K92 data plot off the accumulation line, near the stage II annealing line, which represents the limit for the ω_1, ω_3, and ω_{ER} data (Figure 3; orange). The ω–ω plots are more efficient than the ω–Γ plots for detecting zircons with stage I or stage II annealing. However, the separation between the accumulation and annealing lines decreases with increasing ω, and makes it difficult to distinguish between zircons with little accumulated damage and those with advanced stage II annealing.

Partial annealing can also be detected by comparing the calculated damage estimates for different bands (D; Equation 1; Table 1). Figure 4 shows D–D plots (damage vs. damage) for K86, K92, and FC1 based on Γ_2, Γ_3, and Γ_{ER} (Γ_1 is difficult to measure with precision): (a) D_{ER} versus D_2, (b) D_{ER} versus D_3, and (c) D_3 versus D_2. Unannealed

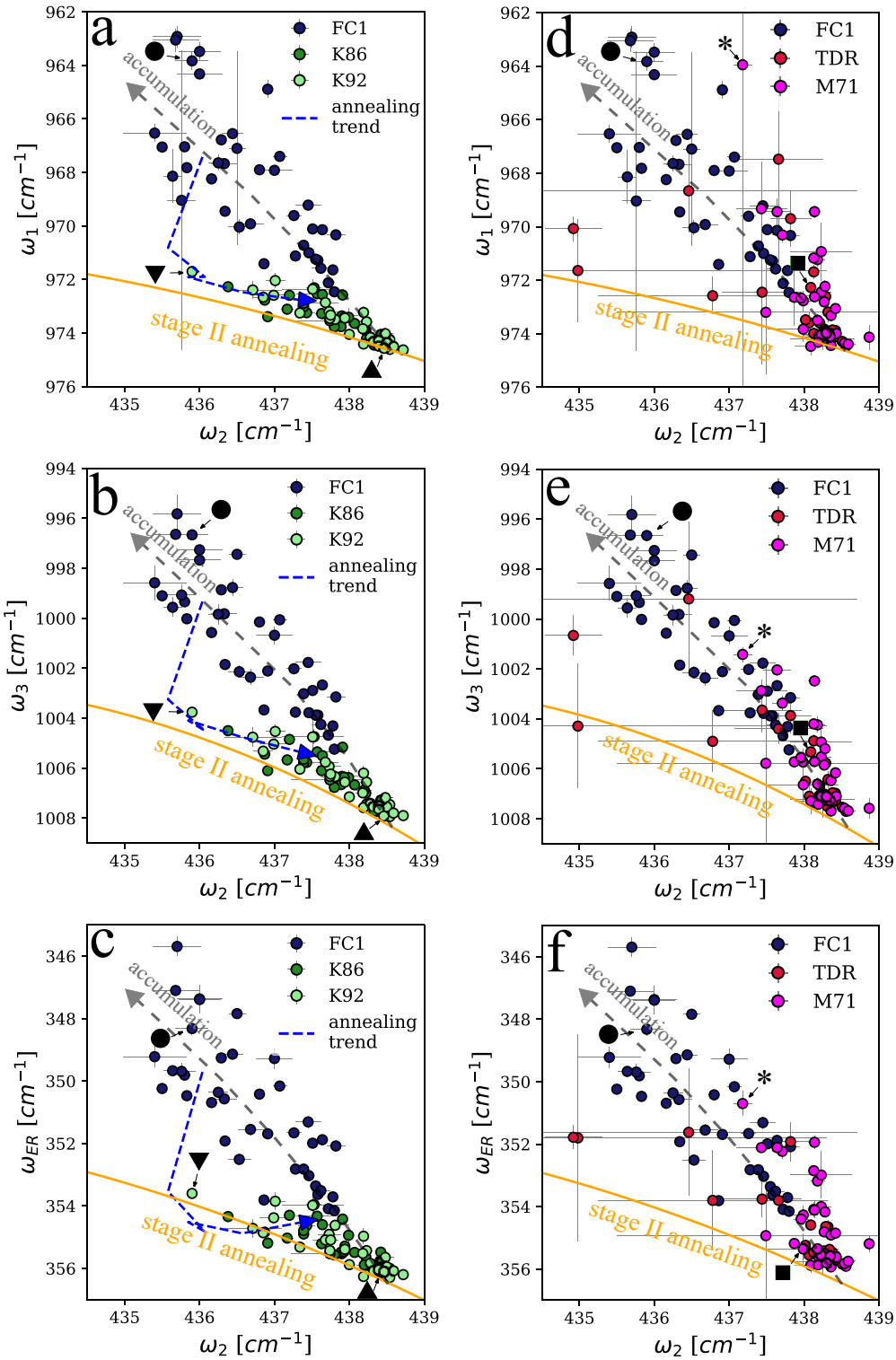

Figure 3. ω–ω plots with inverted vertical axes of (a) $\nu_1(SiO_4)$ and $\nu_2(SiO_4)$, (b) $\nu_3(SiO_4)$ and $\nu_2(SiO_4)$, and (c) external rotation (ER) and $\nu_2(SiO_4)$ of the partially annealed samples K86 and K92; and of (d) $\nu_1(SiO_4)$ and $\nu_2(SiO_4)$, (e) $\nu_3(SiO_4)$ and $\nu_2(SiO_4)$, and (f) ER and $\nu_2(SiO_4)$ of the samples TDR and M71 showing band overlap. Sample FC1 is shown in every plot for comparison. The gray dashed lines are the radiation-damage accumulation trends. The blue dashed lines are the isothermal annealing trajectories as in Figure 2. The orange line is the stage II annealing trend of Härtel, Jonckheere, Wauschkuhn, and Ratschbacher (2021). Symbols ▲, ▼, ■, ✻, and ● mark the data points corresponding to the spectra in Figure 1. Error bars are 2σ.

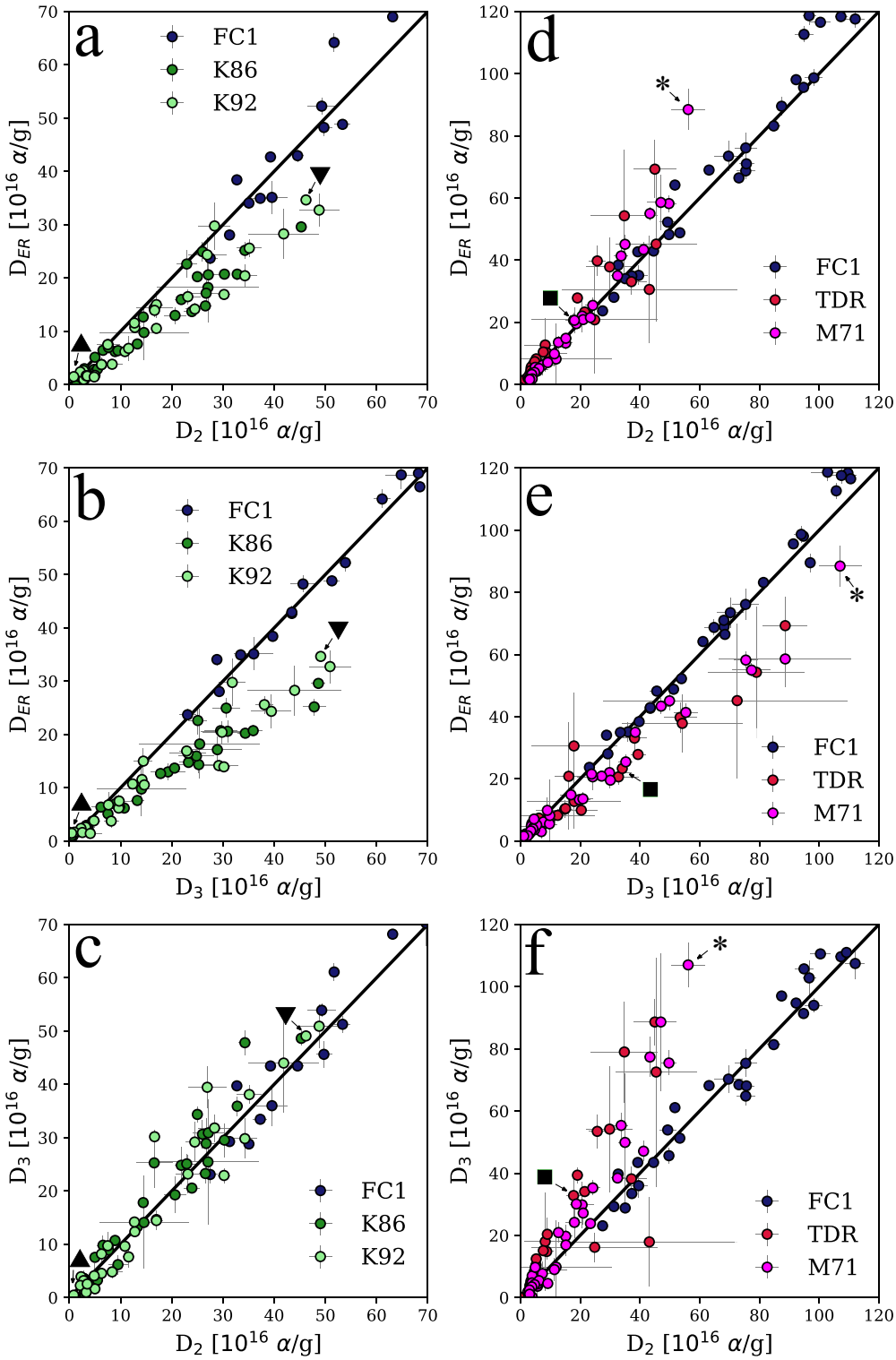

Figure 4. *D*–*D* (damage vs. damage) plots calculated from the $\nu_2(SiO_4)$, $\nu_3(SiO_4)$, and ER bandwidths using Equation 1. The left side shows (a) D_{ER} versus D_2, (b) D_{ER} versus D_3, and (c) D_3 versus D_2 plots for the partially annealed samples K86 and K92. The right side shows (d) D_{ER} versus D_2, (e) D_{ER} versus D_3, and (f) D_3 versus D_2 plots for the band-overlap samples TDR and M71. FC1 is shown in all plots for comparison. Symbols ▲, ▼, ■, ✻, and ● mark the data points corresponding to the spectra in Figure 1. Error bars are 2σ.

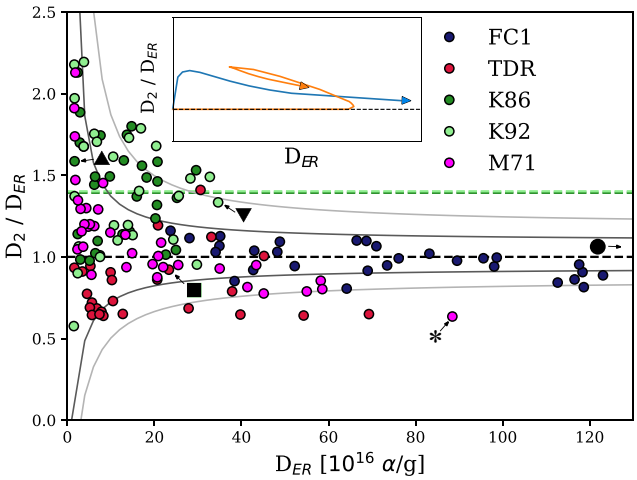

Figure 5. D_2/D_{ER}–D_{ER} plots with 90% (dark gray), and 99% (light gray) prediction intervals for 4% relative errors on Γ (1σ). Dashed lines indicate the unity ratio expected for unannealed zircon (black), and the ratio of mean D values for the partially annealed samples K86 and K92 (greens). The samples TDR, M71, and FC1 are shown for comparison. Symbols ▲, ▼, ■, ✻, and ● mark the data points corresponding to the spectra in Figure 1. The inset shows a schematic slow cooling (blue) and reheating (orange) path in D_2/D_{ER}–D_{ER} space (Text S3 in Supporting Information S1).

zircons plot along lines with unit slope, as $D_2 = D_3 = D_{ER} = D_\alpha$. The Raman bands have different dose responses but also different annealing rates (Härtel, Jonckheere, Wauschkuhn, & Ratschbacher, 2021): during annealing Γ_{ER} reduces about twice as fast as Γ_2 and Γ_3, thus $D_{ER} < D_2 \approx D_3 < D_\alpha$. Accordingly, K86 and K92 plot below the 1:1 line in the D_{ER}–D_2 (Figure 4a) and D_{ER}–D_3 plots (Figure 4b) but close to the 1:1 line in a D_3-D_2 plot (Figure 4c); the unannealed FC1 sample plots on the 1:1 line in all plots.

The D_2/D_{ER}-ratio is useful for detecting partial annealing, on condition that we distinguish systematic deviations from 1 due to annealing from random deviations due to measurement errors. It follows from Equation 1 that, as $D \to 0$, $\Gamma - \Gamma_0 \to 0$; measurement errors on Γ thus produce increasing relative errors on D as D decreases. Figure 5 plots D_2/D_{ER} against D_{ER}. The black dashed line at $D_2/D_{ER} = 1$ corresponds to no annealing. We estimated the statistical error on D_2/D_{ER} as a function of D_{ER} based on 4% (1σ) measurement errors on Γ_2 and Γ_{ER}, which is the average of the present data. The prediction intervals indicate the ranges within which 90% (dark gray) and 99% (light gray) of the data fall if the variation of the D_2/D_{ER}-ratio is due to random measurement errors alone.

Most FC1 data plot within the prediction bands but a large fraction of the K86 and K92 data plot outside it, at $D_2/D_{ER} > 1$. Measurement errors cannot account for their elevated D_2/D_{ER}-ratios. The ratios of the average D_2 and D_{ER} values are both around ~1.5 (Figure 5; green dashed lines). The K86 and K92 data inside the prediction bands (e.g., sample ▲ from Figure 1a) are due to random effects counterbalancing the systematic effect: these grains have been annealed but the effect cannot be separated from statistical measurement errors. The D_2/D_{ER}–D_{ER} plot permits to recognize a partially annealed population but not individual grains. If a higher proportion of the data lies outside the prediction boundaries than expected from chance, the population is assumed to have been annealed.

In principle, the D_2/D_{ER}–D_{ER} plot allows to distinguish thermal histories. The inset in Figure 5 shows two cases: gradual cooling (blue) and a late partial reset (orange). Both plot above $D_2/D_{ER} = 1$. In the case of gradual cooling through the radiation damage partial annealing zone, D_{ER} increases over time and $D_2/D_{ER} > 1$ due to annealing. At lower temperatures, damage accumulation further increases D_{ER}, but decreases D_2/D_{ER} because it dilutes the earlier annealing signature. The longer the sample resides in the total retention zone, the closer D_2/D_{ER} approaches to 1. D_2/D_{ER} does not peak at the initial maximum temperature, because D_2/D_{ER} decreases rather than increases during advanced stage II annealing (Härtel, Jonckheere, Wauschkuhn, & Ratschbacher, 2021). In the case of reheating, the sample evolves toward increasing D_{ER} along $D_2/D_{ER} = 1$ as long as no annealing takes place. The heating event causes loss of damage so that D_{ER} decreases while D_2/D_{ER} increases. During cooling after reaching the peak temperature, there is renewed net damage accumulation, and the path reverts toward increasing D_{ER} while D_2/D_{ER} decreases, as for the cooling path. The final D_{ER} value depends on the damage accumulated prior to annealing, the peak-temperature conditions, the cooling rate, and the residence time at surface temperatures. We discuss the time-temperature conditions for the paths shown in Figure 5 and the possibilities of radiation-damage modeling in Text S3 in Supporting Information S1.

3.2. Band Overlap From Mixed Signals

The TDR and M71 data plot close to the accumulation trends in Figures 2e–2h and 3d–3f, except for scattered outliers due to imprecise measurements. The large errors are due to substantial differences between the four measurements around each spot. TDR and M71 are off the 1:1 lines in the three D-D plots: $D_3 > D_{ER} > D_2$ (Figures 4d–4f). We interpret this offset as the result of overlapping signals from parts of the sampled volume with contrasting damage densities (Figure 6). This causes an averaging of the true peak positions but, above all, an overestimation of the bandwidth relative to the true bandwidths of the component signals. Narrow Raman bands are more affected than those with greater widths. Figure 6 shows the simulated overlap (black) of background-corrected Raman spectra at $D \approx 4{\cdot}10^{16}$ α/g (blue) and $45{\cdot}10^{16}$ α/g (orange). Broadening and asymmetry

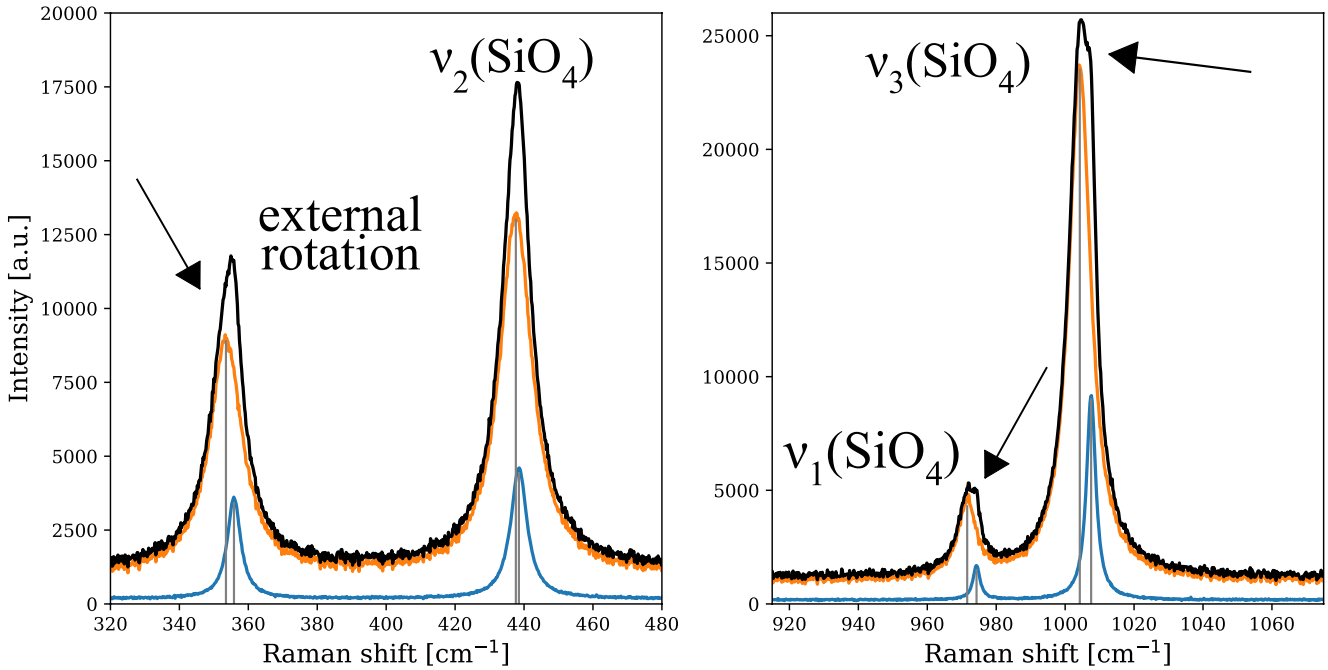

Figure 6. Spectra of two zircon grains at $D \approx 4{\cdot}10^{16}$ (blue, TDR) and $45{\cdot}10^{16}$ α/g (orange, FC1) and their sum (black). Vertical gray lines indicate the band positions of the two spectra. The arrows point to visibly asymmetric bands in the mixed spectrum. The two spectra are marked in Table S1. Band assignment after Kolesov et al. (2001).

are most pronounced for the narrow $\nu_1(SiO_4)$ and $\nu_3(SiO_4)$ bands; the ER band is slightly left-skewed, whereas $\nu_2(SiO_4)$ appears unaffected. This means that overlap leads to higher Γ_3 ages than those calculated from Γ_{ER} and Γ_2.

The apparent position and width, and thence the associated apparent damage of a composite peak have a complicated relationship with the peak parameters of their components. On first order, they depend on the widths of the affected band and the distance between its positions in the two components, which depends on the shift rate $\Delta\omega/\Delta D$. The FC1 data in Figure 2 and the values in Table 1 show that $\nu_1(SiO_4)$ and $\nu_3(SiO_4)$ are narrow and have the highest $\Delta\omega/\Delta D$, while by ER and $\nu_2(SiO_4)$ are broader and shift less. $\nu_1(SiO_4)$ and $\nu_3(SiO_4)$ are narrow and broaden at low rates, whereas $\nu_2(SiO_4)$ and ER are broader and broaden at higher rate. This is illustrated in Figure 6, where band overlap strongly affects $\nu_1(SiO_4)$ and $\nu_3(SiO_4)$, because of their difference in position between the $4{\cdot}10^{16}$ and $45{\cdot}10^{16}$ α/g spectra (vertical lines) relative to their Γ. ER and $\nu_2(SiO_4)$, in contrast, are less separated and show higher widths. This explains the difference in D due to overlap.

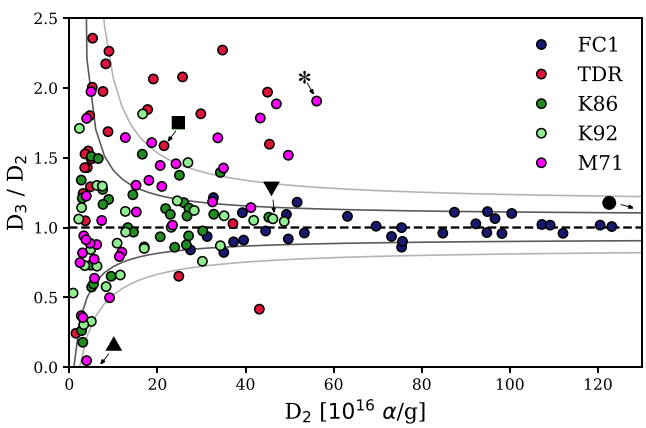

Figure 7. D_3/D_2–D_2 plot with 90% (dark gray), and 99% (light gray) prediction intervals for 4% relative errors on Γ (1σ). The black dashed line indicates the expected ratio. The samples FC1, K86, and K92 are shown for comparison. Symbols ▲, ▼, ■, ✻, and ● mark the data points corresponding to the spectra in Figure 1.

Figure 6 shows a simple case with two separate components, but the spectrum can include more components, for example, in the case of fine growth zoning. Radiation-damage halos, formed by α-particles ejected from a high-eU zone, create a continuous damage gradient (Nasdala et al., 2005). Here, the damage decreases with the distance from the zone boundary and a measurement within the halo sums the Raman signals from a continuum. In such cases, we expect a similar overlap effect on the different Raman bands.

Multi-band measurements permit to detect overlap in a similar manner as annealing. In contrast to annealing, which affects the entire grain population, overlap must be evaluated on a grain-by-grain basis. Following the same procedure, we use the ratio of damage estimates from the most and the least affected Raman bands and compare it to the statistical uncertainties. Figure 7 plots D_3/D_2 against D_2. Several TDR and M71 grains, including

those in Figures 1c and 1d, fall outside the prediction bands, that is, their D_3/D_2-ratios are higher than can be accounted for by analytical error alone. In contrast, most K86, K92, and FC1 data are within the statistical limits, consistent with the fact that Γ_2 and Γ_3 have similar annealing sensitivities (Härtel, Jonckheere, Wauschkuhn, & Ratschbacher, 2021).

In contrast to partial annealing, overlap lowers the D_2/D_{ER}-ratios (Figure 5). Measurements affected by overlap *and* partial annealing can therefore plot within the acceptance interval in a D_2/D_{ER}–D_{ER} plot. However, the D_3/D_2–D_2 plot is not affected by annealing and reveals overlap in such cases. Both D/D-D plots are thus necessary to detect both systematic effects. In Appendix A, we present a workflow for zircon Raman dating that integrates the D_3/D_2 and D_2/D_{ER}-ratio into the procedure.

Estimating radiation-damage components from Raman bands broadened by overlap is difficult. Nasdala et al. (2002) and Kempe et al. (2018) fitted several peaks to a single $\nu_3(SiO_4)$ band. However, due to trade-offs between the parameters (positions, widths, and intensities), the fitted values may not correspond to real damage components. For the present, the safest course of action is to discard such data.

3.3. *D/D*-Ratio Maps

Zircon Raman maps are a useful tool for visualizing the intra-grain distribution of radiation damage. In particular, D_2/D_{ER}-ratio maps help to determine the state of annealing within a single grain, and D_3/D_2-ratio maps guide the evaluation of the effects of zoning on zircon Raman spectra. Figure 8 shows CL and Raman maps of a mm-sized Plešovice zircon. The CL image (Figure 8a) reveals a faint, patchy pattern in the cracked core and faint, concentric oscillatory zoning in the rim, which also encloses two patchy, lighter domains. Figure 8b maps Γ_{ER}, revealing radiation-damage zoning with a similar pattern as in the CL image. The well-ordered core is surrounded by a moderately damaged band and a slightly damaged outer rim. The strongest damage occurs in the grain's pyramidal zone at the lower right, where Γ_{ER} reaches 40 cm^{-1}. Despite its limited resolution (30 μm), the Γ_{ER} map shows the oscillatory zoning of the rim and the cracks in the core.

Figure 8c maps the D_3/D_2-ratios; over most of the area, D_3/D_2 varies between 0.8 and 1.2, indicating little or no band overlap. The areas of elevated D_3/D_2, in particular around the cracked rim on the right, are unsuitable for Raman measurement. Elevated D_3/D_2 also occur in small areas near the core-rim boundary on the left. The low-D_3/D_2 (Figure 8c) and low damage (Figure 8b) areas in the rim correspond to the lighter CL domains (Figure 8a). Figure 8d maps D_2/D_{ER}, with values between 0.9 and 1.2 across the core and rim, except for the cracked area on the right. The brighter zones in CL have low D_3/D_2 and elevated D_2/D_{ER}, due to an elevated D_2 compared to D_3 and D_{ER}. We conjecture that these are recrystallized areas, hence also the low Γ_{ER}. These domains are best avoided for dating due to their indistinct patchy CL and radiation-damage characteristics. The uniform D_2/D_{ER}-ratio near 1 indicates that no significant partial annealing has taken place during the cooling of the Plešovice granulite.

Raman (ω, Γ) and D/D-ratio maps visualize the damage distribution in a zircon grain, permitting to detect partial annealing and measurement artifacts due to overlap. This offers the prospect of matching Raman maps with eU maps and to calculate ages at the most suitable locations. Zoned grains with a wide range of Γ and eU allow to fit a single-grain isochron (Härtel, Jonckheere, Wauschkuhn, Hofmann, et al., 2021). Single-grain Raman ages are important when few grains are available, including dating of thin sections, extra-terrestrial samples, and sediments containing grains from different source areas. Radiation-damage maps also give useful indications for spatially resolved U/Pb and (U-Th)/He dating. For example, these methods should avoid the highly damaged zone in Figure 8b, because of possible Pb or He loss (Danišik et al., 2017; Nasdala et al., 1998). Although Raman mapping is more time-consuming than single spot measurements, it gives a better insight into the intra-grain distribution of radiation damage and guides the spot selection for further measurements on the analyzed grains.

4. Conclusions

Our examples illustrate the advantages of multi-band zircon Raman measurements for revealing partial annealing and band overlap. The zircon internal stretching ($\nu_1(SiO_4)$, $\nu_3(SiO_4)$), and bending ($\nu_2(SiO_4)$) Raman bands and the ER band have been calibrated previously to give consistent estimates of the accumulated radiation damage, corresponding to the calculated α-dose ($D_1 = D_2 = D_3 = D_{ER} = D_\alpha$; Härtel, Jonckheere, Wauschkuhn, Hofmann, et al., 2021). These bands exhibit different sensitivities to annealing (Härtel, Jonckheere, Wauschkuhn,

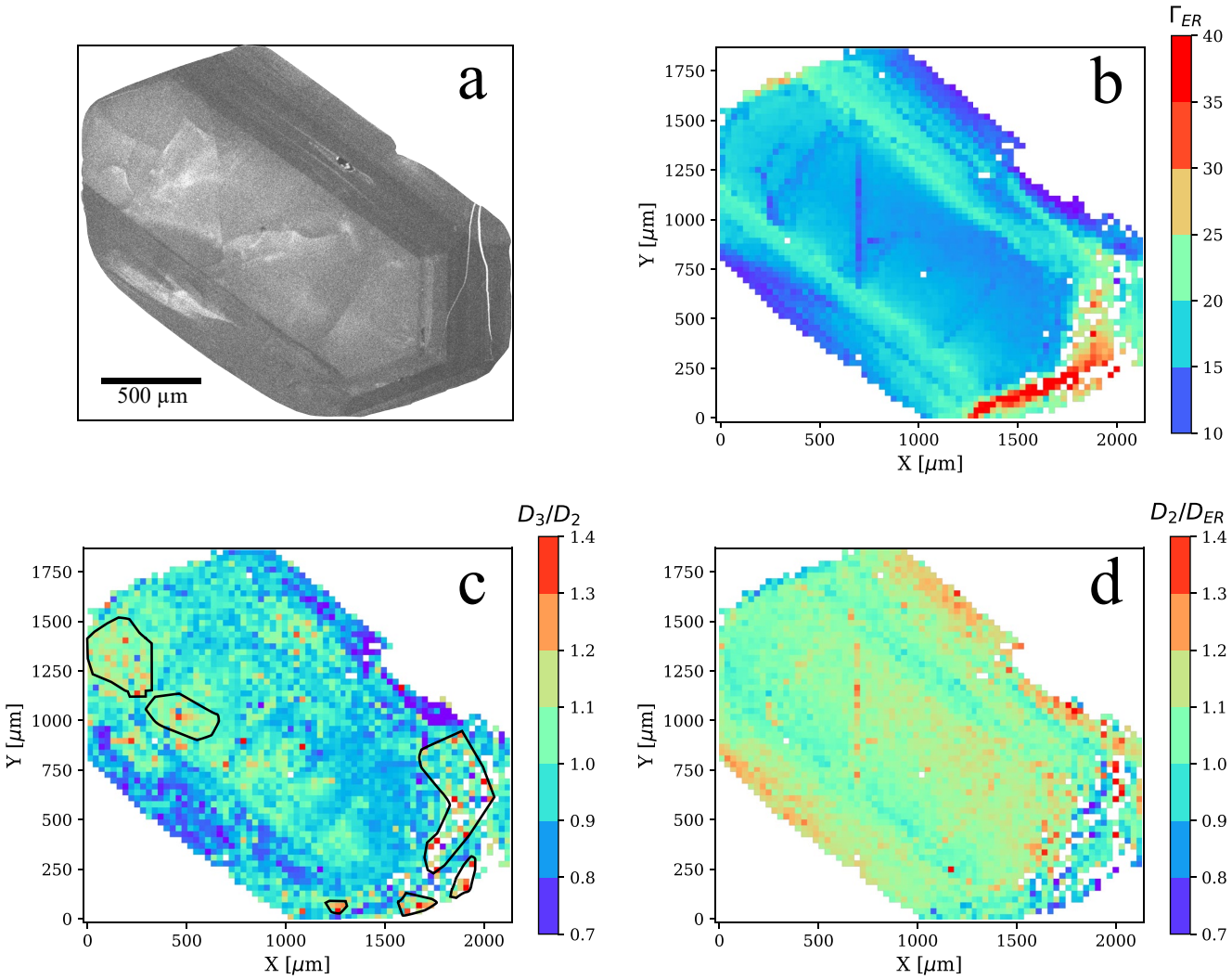

Figure 8. Maps of Plešovice zircon. (a) Cathodoluminescence image. (b) Map of Γ_{ER}. White pixels indicate spectra left out due to low signal-to-noise ratios. (c) D_3/D_2 map. Areas of elevated ratios are marked in black. (d) D_2/D_{ER} map.

& Ratschbacher, 2021): the ER band is most sensitive to annealing, whereas $\nu_2(SiO_4)$ and $\nu_3(SiO_4)$ have similar annealing rates ($D_{ER} < D_2 \approx D_3$, and $D_2/D_{ER} > 1$). In a D_2/D_{ER}–D_{ER} plot, an annealed grain population plots above the $D_2/D_{ER} = 1$ line. A D_2/D_{ER} average well above 1 and/or a significant fraction of the grains outside the statistical limits of the measurement errors indicate that the entire population should be considered as having experienced partial annealing. The annealing trajectories are also distinct in position-bandwidth (ω-Γ) plots of $\nu_1(SiO_4)$ and $\nu_2(SiO_4)$ but less in those of $\nu_3(SiO_4)$ and ER. In ω–ω plots of $\omega_1(SiO_4)$, $\omega_3(SiO_4)$, and ω_{ER} against $\omega_2(SiO_4)$, a partially annealed grain population shows a collective offset away from the accumulation trend toward the ω–ω line for stage-II annealing.

In zoned zircons, the sampled volume may include different damage densities, producing superimposed, and therefore broadened bands. The fact that overlap affects the Raman bands to a different extent offers a means of detecting mixed signals. The difference between the broad $\nu_2(SiO_4)$ band and the narrow $\nu_3(SiO_4)$ band is most marked because of their contrasting widths (Γ) and downshift. The D_3/D_2-ratio is thus a good indicator of a mixed signal. A D_3/D_2–D_2 plot is useful for distinguishing the systematic overlap effect from statistical scatter. Results exceeding the statistical tolerances should be excluded on a grain by grain basis. Multi-band Raman maps can be converted to D/D-ratio maps and interpreted in terms of overlap and annealing. The example of the Plešovice zircon illustrates that these maps can be used for selecting the best spot positions for single-grain zircon Raman

dating. Multi-band Raman analysis is thus a useful approach for radiation-damage measurements, for Raman dating, or damage characterization for (U-Th)/He dating and detrital geo-thermochronology.

Appendix A: Measurement Protocol for Zircon Raman Dating

Figure A1 presents a measurement protocol for zircon Raman dating. It comprises three steps: preparation, measurement, and evaluation. Sample preparation involves separating, mounting, and polishing the zircon sample, and the acquisition of images (CL, BSE, and reflected light) for archiving and selecting measurement spots. The screening must take the spot sizes of the Raman microprobe and the eU measurement (LA-ICP-MS, EPMA, or SIMS) into account and set spots in areas that are homogeneous at both scales. One strategy is to map with the Raman probe an area the size of the eU measurement spot. It is advantageous to place spots in areas with different CL or BSE intensities, so that the Raman and eU results cover a broad range of radiation-damage densities for isochron dating (Härtel, Jonckheere, Wauschkuhn, Hofmann, et al., 2021).

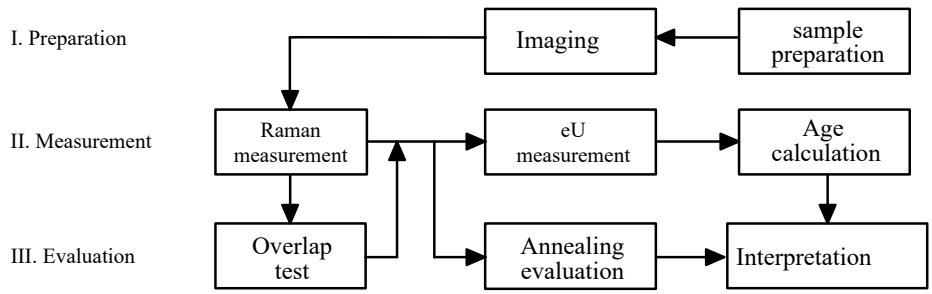

Figure A1. Flow chart of the zircon Raman-dating procedure.

The non-destructive Raman measurements are carried out before the eU measurements. It is useful to map zoned grains with the Raman probe for comparing the damage distribution with the CL and/or BSE images. Different damage estimates are calculated from the Raman bandwidths with Equation 1 and the values in Table 1. These data permit an evaluation of the sample before the eU measurement. A D_3/D_2–D_2 plot or a D_3/D_2 map is used for detecting band overlap artifacts; spots or areas with D_3/D_2 values outside the prediction boundaries are excluded. Occasional band overlap is almost inevitable in maps of zoned zircon. However, the spectrum of each data point outside the boundaries should be examined before removing it from the data set. To construct the prediction boundaries, the analyst estimates the relative uncertainties of their Γ measurements and chooses a confidence level for accepting or rejecting data. Assuming $D_2 = D_3$ for undisturbed measurements, the upper prediction boundary is calculated as a function of D_2:

$$\frac{D_3}{D_2}^{upper} = \frac{D_2(1 + k\sigma_3) - \dfrac{\Gamma_{0;3}}{\Delta\Gamma_3/\Delta D}}{D_2(1 - k\sigma_2) - \dfrac{\Gamma_{0;2}}{\Delta\Gamma_2/\Delta D}}, \tag{A1}$$

wherein σ_2 and σ_3 are the relative standard deviations of Γ_2 and Γ_3, with k depending on the confidence level (~90% for $k = 1$; ~99% for $k = 2$). Inserting the zero-damage bandwidths and dose responses from Table 1 gives:

$$\frac{D_3}{D_2}^{upper} = \frac{D_2(1 + k\sigma_3) - 25.9(10^{16}\alpha/\mathrm{g})}{D_2(1 - k\sigma_2) - 36.9(10^{16}\alpha/\mathrm{g})}. \tag{A2}$$

For the lower boundary, we have that:

$$\frac{D_3}{D_2}^{lower} = \frac{D_2(1 - k\sigma_3) - 25.9(10^{16}\alpha/\mathrm{g})}{D_2(1 + k\sigma_2) - 36.9(10^{16}\alpha/\mathrm{g})}. \tag{A3}$$

The eU-measurement is followed by the calculation of the Raman age from D and eU using Equation 2. Härtel, Jonckheere, Wauschkuhn, Hofmann, et al. (2021) proposed three methods for calculating a population age: a weighted mean, pooled, or isochron age. The D_2/D_{ER}–D_{ER} plot provides information on the state of annealing of

the population, important for interpreting the Raman age. The upper and lower boundaries are constructed as for the D_3/D_2-D_2 plot, assuming $D_2 = D_{ER}$ for unannealed zircon:

$$\frac{D_2}{D_{ER}}^{upper} = \frac{D_{ER}(1+k\sigma_2) - \frac{\Gamma_{0;2}}{\Delta\Gamma_2/\Delta D}}{D_{ER}(1-k\sigma_{ER}) - \frac{\Gamma_{0;ER}}{\Delta\Gamma_{ER}/\Delta D}}$$

$$= \frac{D_{ER}(1+k\sigma_2) - 36.9(10^{16}\alpha/g)}{D_{ER}(1-k\sigma_{ER}) - 23.8(10^{16}\alpha/g)}, \quad \text{(A4)}$$

$$\frac{D_2}{D_{ER}}^{lower} = \frac{D_{ER}(1-k\sigma_2) - 36.9(10^{16}\alpha/g)}{D_{ER}(1+k\sigma_{ER}) - 23.8(10^{16}\alpha/g)}. \quad \text{(A5)}$$

If most D_2/D_{ER}-ratios are within the prediction bands, the age is either an event, a reset, or a cooling age. If more ratios are outside the boundaries than allowed by statistical uncertainty, then partial annealing is suspected. In this case, the age is either a mixed age or the sample has experienced slow cooling. The proposed protocol is also appropriate for Raman applications in zircon (U-Th)/He dating and zircon provenance studies.

Conflict of Interest

The authors declare no conflicts of interest relevant to this study.

Data Availability Statement

Supporting Information is available (CC-BY 4.0 license) on the OpARA server of TU Bergakademie Freiberg and TU Dresden at http://dx.doi.org/10.25532/OPARA-155.

Acknowledgments
The authors thank Hideki Iwano and Kyoto Fission-Track Ltd. for providing sample TDR, Hideki Iwano and Masa Ogasawara for providing sample FC1, and Jiři Sláma for providing the Plešovice zircon. Birk Härtel was supported by the German scholarship foundation (Studienstiftung des deutschen Volkes). The authors thank Alberto Resentini and two anonymous reviewers for their helpful comments on the manuscript. The authors thank Peter van der Beek for editorial handling.

References

Anderson, A. J., Hanchar, J. M., Hodges, K. V., & van Soest, M. C. (2020). Mapping radiation damage zoning in zircon using Raman spectroscopy: Implications for zircon chronology. *Chemical Geology*, *538*, 119494. https://doi.org/10.1016/j.chemgeo.2020.119494

Bohr, N. (1948). The penetration of atomic particles through matter. *Det Kongelige Danske Videnskabernes Selskab Mathematisk-fysiske Meddelelser*, *XVIII*(8), 144.

Colombo, M., & Chrosch, J. (1998). Annealing of natural metamict zircons. I low degree of radiation damage. *Radiation Physics and Chemistry*, *53*, 555–561. https://doi.org/10.1016/s0969-806x(98)00193-5

Danišik, M., McInnes, B. I. A., Kirkland, C. L., McDonald, B. J., Evans, N. J., & Becker, T. (2017). Seeing is believing: Visualization of He distribution in zircon and implications for thermal history reconstruction on singles crystals. *Science Advances*, *3*, e1601121. https://doi.org/10.1126/sciadv.1601121

Dodson, M. H. (1973). Closure temperature in cooling geochronological and petrological systems. *Contributions to Mineralogy and Petrology*, *40*, 259–274. https://doi.org/10.1007/bf00373790

Ganerød, M., Chew, D. M., Smethurst, M. A., Troll, V. R., Corfu, F., Meade, F., & Prestvik, T. (2011). Geochronology of the Tardree Rhyolite Complex, Northern Ireland: Implications for zircon fission track studies, the North Atlantic Igneous Province and the age of the Fish Canyon sanidine standard. *Chemical Geology*, *286*, 222–228. https://doi.org/10.1016/j.chemgeo.2011.05.007

Garver, J. I., & Davidson, C. M. (2015). Southwestern Laurentian zircons in upper Cretaceous flysch of the Chugach-Prince William terrane in Alaska. *American Journal of Science*, *315*, 537–556. https://doi.org/10.2475/06.2015.02

Geisler, T. (2002). Isothermal annealing of partially metamict zircon: Evidence for a three-stage recovery process. *Physics and Chemistry of Minerals*, *29*, 420–429. https://doi.org/10.1007/s00269-002-0249-3

Geisler, T., & Pidgeon, R. T. (2002). Raman scattering from metamict zircon: Comments on "Metamictisation of natural zircon: Accumulation versus thermal annealing of radioactivity-induced damage" by Nasdala et al. (2001, *Contributions to Mineralogy and Petrology* 141: 125–144). *Contributions to Mineralogy and Petrology*, *143*, 750–755. https://doi.org/10.1007/s00410-002-0378-1

Geisler, T., Pidgeon, R. T., Van Bronswijk, W., & Pleysier, R. (2001). Kinetics of thermal recovery and recrystallization of partially metamict zircon: A Raman spectroscopic study. *European Journal of Mineralogy*, *13*, 1163–1176. https://doi.org/10.1127/0935-1221/2001/0013-1163

Ginster, U. (2018). *The effects of radiation damage accumulation and annealing on helium diffusion in zircon* (PhD dissertation, p. 340). The University of Arizona.

Ginster, U., Reiners, P. W., Nasdala, L., & Chanmuang, N. C. (2019). Annealing kinetics of radiation damage in zircon. *Geochimica et Cosmochimica Acta*, *249*, 225–246. https://doi.org/10.1016/j.gca.2019.01.033

Green, P. F. (1985). Comparison of zeta calibration baselines for fission-track dating of apatite, zircon and sphene. *Chemical Geology*, *58*, 1–22. https://doi.org/10.1016/0168-9622(85)90023-5

Guenthner, W. R., Reiners, P. W., Ketcham, R. A., Nasdala, L., & Giester, G. (2013). Helium diffusion in natural zircon: Radiation damage, anisotropy, and the interpretation of zircon (U-Th)/He thermochronology. *American Journal of Science*, *313*, 145–198. https://doi.org/10.2475/03.2013.01

Härtel, B., Jonckheere, R., Wauschkuhn, B., Hofmann, M., Frölich, S., & Ratschbacher, L. (2021a). Zircon Raman dating: Age equation and calibration. *Chemical Geology*, *579*, 120351. https://doi.org/10.1016/j.chemgeo.2021.120351

Härtel, B., Jonckheere, R., Wauschkuhn, B., & Ratschbacher, L. (2021b). The closure temperature(s) of zircon Raman dating. *Geochronology*, *3*, 259–272. https://doi.org/10.5194/gchron-3-259-2021

Holland, H. D., & Gottfried, D. (1955). The effect of nuclear radiation on the structure of zircon. *Acta Crystallographica*, *8*, 291–300. https://doi.org/10.1107/s0365110x55000947

Hueck, M., Dunkl, I., Heller, B., Stipp Basei, M. A., & Siegesmund, S. (2018). (U-Th)/He thermochronology and zircon radiation damage in the South American passive margin: Thermal overprint of the Paraná LIP? *Tectonics*, *37*, 4068–4085. https://doi.org/10.1029/2018tc005041

Hurford, A. J. (1990). Standardization of fission track dating calibration: Recommendation by the Fission Track Working Group of the I.U.G.S. Subcommission on Geochronology. *Chemical Geology: Isotope Geoscience section*, *80*(2), 171–178. https://doi.org/10.1016/0168-9622(90)90025-8

Hurford, A. J., & Green, P. F. (1983). The zeta age calibration of fission-track dating. *Chemical Geology*, *41*, 285–317. https://doi.org/10.1016/s0009-2541(83)80026-6

Iwano, H., Danhara, T., Yuguchi, T., Hirata, T., & Ogasawara, M. (2019). Duluth Complex apatites: Age reference material for LA-ICP-MS-based fission-track dating. *Terra Nova*, *31*(3), 247–256. https://doi.org/10.1111/ter.12393

Joly, J. (1907). XXIX. Pleochroic halos. *London, Edinburgh and Dublin Philosophical Magazine and Journal of Science*, *13*, 381–383. https://doi.org/10.1080/14786440709463613

Jonckheere, R., & Gögen, K. (2001). A Monte-Carlo calculation of the size distribution of latent α-recoil tracks. *Nuclear Instruments and Methods in Physics Research B*, *183*, 347–357. https://doi.org/10.1016/s0168-583x(01)00691-7

Jonckheere, R., Heinz, D., Hacker, B. R., Rafaja, D., & Ratschbacher, L. (2019). A borehole investigation of zircon radiation damage annealing. *Terra Nova*, *31*, 263–270. https://doi.org/10.1111/ter.12395

Kempe, U., Trullenque, G., Thomas, R., Sergeev, S., Presnyakov, S., Rodionov, N., & Himcinschi, C. (2018). Substitution-induced internal strain and high disorder in weakly radiation damaged hydrothermal zircon from Mt. Malosa, Malawi. *European Journal of Mineralogy*, *30*, 659–679. https://doi.org/10.1127/ejm/2018/0030-2739

Kolesov, B. A., Geiger, C. A., & Armbruster, T. (2001). The dynamic properties of zircon studied by single-crystal X-ray diffraction and Raman spectroscopy. *European Journal of Mineralogy*, *13*, 939–948. https://doi.org/10.1127/0935-1221/2001/0013-0939

Marillo-Sialer, E., Woodhead, J., Hanchar, J. M., Reddy, S. M., Greig, A., Hergt, J., & Kohn, B. (2016). An investigation of the laser-induced zircon 'matrix effect'. *Chemical Geology*, *438*, 11–24. https://doi.org/10.1016/j.chemgeo.2016.05.014

Mügge, O. (1922). Über isotrop gewordene Kristalle. *Centralblatt für Mineralogie, Geologie und Paläontologie Jg*, *1922*, 721–739.

Murakami, T., Chakoumakos, B. C., Ewing, R. C., Lumpkin, G. R., & Weber, W. J. (1991). Alpha-decay event damage in zircon. *American Mineralogist*, *76*, 1510–1532.

Nasdala, L., Hanchar, J. M., Kronz, A., & Whitehouse, M. (2005). Long-term stability of alpha particle damage in natural zircon. *Chemical Geology*, *220*, 83–103. https://doi.org/10.1016/j.chemgeo.2005.03.012

Nasdala, L., Irmer, G., & Jonckheere, R. (2002). Radiation damage ages: Practical concept or impractical vision? – Reply to two comments on "Metamictisation of natural zircon accumulation versus thermal annealing of radioactivity-induced damage", and further discussion. *Contributions to Mineralogy and Petrology*, *143*, 758–765. https://doi.org/10.1007/10.1007/s00410-002-0380-7

Nasdala, L., Irmer, G., & Wolf, D. (1995). The degree of metamictization in zircon: A Raman spectroscopic study. *European Journal of Mineralogy*, *7*, 471–478. https://doi.org/10.1127/ejm/7/3/0471

Nasdala, L., Kostrovitsky, S., Kennedy, A. K., Zeug, M., & Esenkulova, S. A. (2014). Retention of radiation damage in zircon xenocrysts from kimberlites, Northern Yakutia. *Lithos*, *206–207*, 252–261. https://doi.org/10.1016/j.lithos.2014.08.005

Nasdala, L., Pidgeon, R. T., Wolf, D., & Irmer, G. (1998). Metamictization and U-Pb isotopic discordance in single zircons: A combined Raman microprobe and SHRIMP ion probe study. *Mineralogy and Petrology*, *62*, 1–27. https://doi.org/10.1007/bf01173760

Nasdala, L., Wenzel, M., Vavra, G., Irmer, G., & Kober, B. (2001). Metamictisation of natural zircon: Accumulation versus thermal annealing of radioactivity-induced damage. *Contributions to Mineralogy and Petrology*, *141*, 125–144. https://doi.org/10.1007/s004100000235

Paces, J. B., & Miller, J. D. (1993). Precise U-Pb ages of Duluth Complex and related mafic intrusions, northeastern Minnesota: Geochronological insights to physical, petrogenetic, paleomagnetic, and tectonomagmatic processes associated with the 1.1 Ga Midcontinent Rift System. *Journal of Geophysical Research*, *98*, 13997–14013. https://doi.org/10.1029/93jb01159

Pidgeon, R. T. (2014). Zircon radiation damage ages. *Chemical Geology*, *367*, 13–22. https://doi.org/10.1016/j.chemgeo.2013.12.010

Resentini, A., Andò, S., Garzanti, E., Malusà, M. G., Pastore, G., Vermeesch, P., et al. (2020). Zircon as a provenance tracer: Coupling Raman spectroscopy and U-Pb geochronology in source-to-sink studies. *Chemical Geology*, *555*. https://doi.org/10.1016/j.chemgeo.2020.119828

Salje, E. K. H., Chrosch, J., & Ewing, R. C. (1999). Is "metamictization" of zircon a phase transition? *American Mineralogist*, *84*, 1107–1116. https://doi.org/10.2138/am-1999-7-813

Salje, E. K. H., & Farnan, I. (2001). The degree and nature of radiation damage in zircon observed by ^{29}Si nuclear magnetic resonance. *Journal of Applied Physics*, *89*, 2084–2090. https://doi.org/10.1063/1.1343523

Saltonstall, C. B., Beechem, T. E., Amatya, J., Floro, J., Norris, P. M., & Hopkins, P. E. (2019). Uncertainty in linewidth quantification of overlapping Raman bands. *Review of Scientific Instruments*, *90*, 013111. https://doi.org/10.1063/1.5064804

Sláma, J., Košler, J., Condon, D. J., Crowley, J. L., Gerdes, A., Hanchar, J. M., et al. (2008). Plešovice zircon – A new natural reference material for U-Pb and Hf isotopic microanalysis. *Chemical Geology*, *249*, 1–35. https://doi.org/10.1016/j.chemgeo.2007.11.005

Tanabe, K., & Hiraishi, J. (1980). Correction of finite slit width effects on Raman line widths. *Spectrochimica Acta*, *36A*, 341–344. https://doi.org/10.1016/0584-8539(80)80141-3

Trachenko, K., Dove, M. T., & Salje, E. K. H. (2003). Large swelling and percolation in irradiated zircon. *Journal of Physics: Condensed Matter*, *15*, L1–L7. https://doi.org/10.1088/0953-8984/15/2/101

Wagner, G. A. (1981). Fission-track ages and their geological interpretation. *Nuclear Tracks*, *5*, 15–25. https://doi.org/10.1016/0191-278x(81)90022-6

Zhang, M., Salje, E. K. H., Farnan, I., Graeme-Barber, A., Daniel, P., Ewing, R. C., et al. (2000). Metamictization of zircon: Raman spectroscopic study. *Journal of Physics: Condensed Matter*, *12*, 1915–1925. https://doi.org/10.1088/0953-8984/12/8/333